J Mater Sci (2013) 48:8308–8319
DOI 10.1007/s10853-013-7644-7

Characterisation and modelling of the elastic properties of poly(lactic acid) nanofibre scaffolds

Edwin Yesid Gómez-Pachón · Francisco Manuel Sánchez-Arévalo · Federico J. Sabina · Alfredo Maciel-Cerda · Raúl Montiel Campos · Nikola Batina · Israel Morales-Reyes · Ricardo Vera-Graziano

Received: 15 March 2013 / Accepted: 31 July 2013 / Published online: 20 August 2013

Abstract The aim of this study is to predict the elastic response of poly(lactic acid) (PLA) electrospun nanofibre scaffolds through mathematical models based on homogenisation and the differential replacement method (DRM). These models principally seek to determine and analyse the effects of the internal morphology of the nanofibres on the effective Young's modulus of polymer nanofibre scaffolds. The microstructure of the nanofibres was first characterised by SEM, XRD, DSC, AFM, and TEM techniques. From this characterisation, strong evidence of a hierarchical core–shell structure was found. With the experimental data, it was possible to design and validate better models than those currently used. In addition, the effects of the electrospinning parameters, such as take-up velocity and thermal treatment, were analysed and correlated with the morphology and the elastic properties of the nanofibres and their scaffolds. To validate the models' results, we conducted a series of uniaxial tensile tests on the PLA nanofibre scaffolds. Using the data from the nanofibre measurements, the homogenisation approximations and the model based on the DRM predicted an effective Young's modulus of 667 and 835 MPa, respectively. The predicted data were in excellent agreement with the experimental results (685–880 MPa). These models will be useful in understanding and evaluating the structure–property relationships of oriented nanofibre scaffolds for medical or biological applications.

E. Y. Gómez-Pachón · F. M. Sánchez-Arévalo · A. Maciel-Cerda · R. Vera-Graziano (✉)
Instituto de Investigaciones en Materiales, Universidad Nacional Autónoma de México, 04510 Mexico DF, Mexico
e-mail: graziano@unam.mx

E. Y. Gómez-Pachón
e-mail: edwinyesidgom@yahoo.com.mx

F. J. Sabina
Instituto de Investigaciones en Matemáticas Aplicadas y en Sistemas, Universidad Nacional Autónoma de México, 04510 Mexico DF, Mexico

R. M. Campos
Departamento de Polímeros, Universidad Autónoma Metropolitana, Mexico DF, Mexico

N. Batina · I. Morales-Reyes
Laboratorio de Nanotecnología e Ingeniería Molecular, Departamento de Química, Universidad Autónoma Metropolitana, 09340 Mexico DF, Mexico

Introduction

Tissue engineering is one of the most demanding branches of biomedicine and requires that the materials used be productive and innovative. Scaffolds and porous materials produced by several techniques are commonly used in tissue engineering [1]. A common strategy in tissue engineering is the use of biodegradable biomaterials to mimic the functions of native tissues, which may promote cell growth and extracellular matrix generation [2–9] and match the resultant mechanical properties with those of the target tissue. Among the several techniques to produce scaffolds, electrospinning is one of the most useful and versatile methods for controlling the structural parameters of fibrous scaffolds such as the fibre orientation and diameter, texture and scaffold porosity [7–9]. However, our understanding and ability to predict the mechanical properties of electrospun polymer nanofibres are limited.

Some efforts to characterise the mechanical behaviour of fibrous scaffolds used in tissue engineering have been reported by Hong et al. They studied the improvement of the mechanical properties of scaffolds composed of

poly(lactic acid) (PLA) nanofibres obtained by adding hydroxyapatite nanoparticles [10]. Vera et al. [11] reported the effects that grafting PLA chains onto hydroxyapatite nanoparticles had on the scaffold properties, including the effect of fibre randomness on the elastic properties of the scaffolds and on stem cell growth.

An interesting report on the effect of the crystallinity of PLA microfibres under the influence of electrical and centrifugal fields on the mechanical response was described by Liao C-C. et al. [12]. Tan and Lim studied the dependence of the Young's modulus on the diameter of PLA and polycaprolactone (PCL) single nanofibres by atomic force microscopy (AFM) [13–15], and they found that the elastic modulus of the nanofibres increased as the diameter of the nanofibres diminished; a critical diameter was determined for each polymer. Similar effects were also reported by Wong et al. [16] for electrospun PCL and by Naraghi et al. [17] for polyacrylonitrile (PAN) nanofibres . Baji et al. [18] reported the influence of the electrospinning parameters on the morphology and microstructure of several types of nanofibres (PLA, PCL, polyoxymethylene, nylon, cellulose acetate, and others), as well as their mechanical properties. Yoshioka et al. [19] studied the structure of polyethylene (PE) fibres by transmission electron microscopy (TEM). The fibre structure was related to the fibre diameter, and they proposed several different structural models. These results suggest that in randomly deposited nanofibres, as the fibre diameter decreases, there is a higher degree of molecular orientation and crystallinity and improved mechanical properties.

Inai et al. [20] found that the tensile properties of single electrospun PLA nanofibres collected in a rotating disc increased with the take-up velocity (tangential velocity produced by the rotating disc). The elastic behaviour of polymer nanofibres was examined by Arinstein et al. [21] and Cicero et al. [22]; these authors suggested that nanofibres have a supramolecular structure composed of different phases due to their molecular orientation during the electrospinning process. These studies suggested that the structural features of electrospun nanofibres depend on the processing conditions. However, the relationship between the internal structure of nanofibres and their mechanical properties has not been well established.

Some efforts have been addressed to study the mechanical behaviour of collagen networks using the Finite Element Method (FEM) [23, 24]. Sun et al. [25] used the strain gradient theory to model the elastic modulus of polymer nanofibres as a function of fibre diameter with a good approximation. However, these studies did not consider the internal structure of the fibre.

Several authors [26–30] generated explicit solutions for describing the elastic behaviour of a spherical particle or cylindrical fibres with a homogeneous interphase. Shen and Li [31, 32] introduced the differential replacement method (DRM) and applied it to the Mori–Tanaka (MT) formulas to determine the plane bulk modulus K_{23} and longitudinal shear modulus μ_{12} of fibres with an inhomogeneous interphase. Their calculations were compared to the solutions of the FEM with acceptable results. An alternative of the DRM was presented by Sevostianov and Kachanov; they proposed the use of the Hashin–Shtrikman (HS) lower bound formulas for spherical inclusions [33].

The effective Young's modulus of nanofibres has not been determined with enough precision by these models because the semicrystalline structure of the nanofibres is not considered. This work focuses on the development of mathematical models to predict the effective Young's modulus of semicrystalline nanofibre scaffolds based on careful experimental studies of PLA microstructure. The influence of the collection parameters on the crystallinity and mechanical properties of the PLA nanofibres is also considered. The effects of annealing were also studied to determine possible changes in the microstructure and properties of the PLA nanofibres.

Materials and methods

PLA (M_w 230000, NatureWorks 2002D LLC, MN, USA) was dissolved in 2,2,2-trifluoroethanol (Sigma Aldrich) by magnetic stirring to obtain a 16 % (w/v) PLA solution. The PLA solution was electrospun to obtain both randomly and uniaxially oriented nanofibre scaffolds using two different types of collector systems. The electrospinning process was performed at room temperature and pressure, a flow rate of 0.6 ml/h, and an applied voltage of 15 kV (Power supply, Spellman, USA) using a digitally controlled pump (injector, KD Scientific, USA) (see Fig. 1). The collector for the random scaffolds was a 10-cm square aluminium plate. The collector to obtain the oriented nanofibres was a custom-designed aluminium cylinder that rotates at a predetermined velocity in the range of 1–10000 RPM, providing tangential velocities (take-up velocities) ranging between 1 and 3142.6 m/min (52.36 m/s). The nanofibres were collected at 1100 and 1217 m/min. Subsequently, the electrospun scaffolds were kept in desiccators at room temperature. Some scaffolds were annealed at 80 °C for 10 h (Scorpion Scientific, A-50980 oven). The annealing temperature was selected based on the crystallisation temperature of the as-spun aligned nanofibres (approximately 70 °C). In general, annealing takes place at any temperature between the crystallisation temperature and the melting point. The names and abbreviations of the electrospun fibres are shown in Table 1.

The structure of the scaffolds was analysed by scanning electron microscopy (SEM), high-resolution transmission

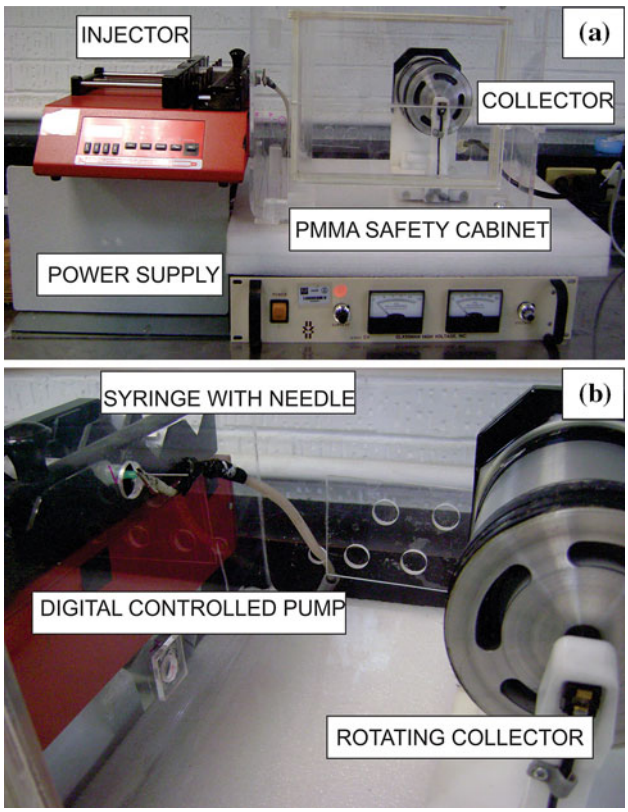

Fig. 1 **a** Electrospinning device used for producing nanofibre scaffolds. **b** Details of the injection collection system

Table 1 Names and abbreviations of the electrospun fibres

Names	Abbreviation
Uniaxially aligned nanofibres	AN
Uniaxially aligned nanofibres collected at 1100 m/min	$AN_{1100\ m/min}$
Uniaxially aligned nanofibres collected at 1217 m/min	$AN_{1217\ m/min}$
Annealed uniaxially aligned nanofibres	A-AN
Annealed uniaxially aligned nanofibres at 1100 m/min	$A\text{-}AN_{1100\ m/min}$
Annealed uniaxially aligned nanofibres at 1217 m/min	$A\text{-}AN_{1217\ m/min}$
Randomly oriented nanofibres	RON
Annealed randomly oriented nanofibres	A-RON

electronic microscopy (HRTEM), X-ray diffraction (XRD), differential scanning calorimetry (DSC) and AFM.

The morphology and distribution of the randomly oriented nanofibres (RONs), aligned nanofibres (ANs) and annealed aligned nanofibres (A-ANs) were observed by SEM (JEOL-JSM-7600F). The operating voltage of the electron beam was 20 kV. The samples were previously coated with gold to increase the conductivity of the surface fibres. The samples were coated under vacuum with a current of 30 mA for 3 min. ImageJ software was used to measure the mean diameter of the nanofibres and the orientation of the ANs. SEM images (10000 ×) at two different locations of each sample were obtained. The diameters of the continuous fibres located at the foreground plane of the micrograph were measured. For the statistical analysis, at least eight points per nanofibre were selected to measure the diameters.

The internal transverse structure of the oriented nanofibres was observed by HRTEM (JEOL-2100f). The samples were embedded in an epoxy resin Epon-812 (Microscopy ScienceR) and cured for 3 days, to impede the fibres from flexing during the cutting process, which was carried out in an Ultracryo Microtome RMCR model MT-7000. A conventional cutting pyramid was prepared, and fine sections (80-nm-thick) were obtained by means of a diamond blade (DIAMONTR) at room temperature, as the T_g for PLA is 60 °C. To obtain the proper contrast for the HRTEM observations, the samples were placed in a chamber under Ru04 vapour for 4 h.

The crystalline structure of the electrospun samples was analysed by XRD (Siemens D-500, Cu K_α radiation; $\lambda = 1.5406$ Å). The scaffolds were carefully sectioned with a cutter in pieces of 1×5 cm^2. Each sample was folded four times to obtain squares that were 1 cm^2 in size and placed on a silica glass. The analysis conditions were as follows: an advance range of 1°/min, the graze angle fixed at 1°, and the detector rotated from 2° to 70°. The diffraction spectrum was indexed by comparison with the Diffract Plus 2005 software.

The thermal transitions in the nanofibres were determined by DSC (2910, TA Instruments). The scaffolds obtained by electrospinning were cut with a puncher. The samples, 0.5 cm in diameter, were encapsulated in an aluminium standard pan. The samples were heated from 0 to 180 °C at a heating rate of 10 °C/min. The thermograms were analysed with the aid of TA Instruments Universal Analysis 2000 software.

The surface of the ANs was observed by AFM (Nanoscope III, Digital Instruments) with a tip model TESP (Si) in the frequency range of 325–382 kHz (Veecoprobes). All images were taken in tapping mode and presented as height and phase images. The samples, 5×5 mm^2, were cut and fixed at the standard AFM sample holder (metal disc). To avoid displacement and mechanical vibration of the nanofibres during the tip movement, a group of a few ANs was approached, and the AFM scan rate was kept below 0.3 Hz.

The mechanical properties were measured under uniaxial tension (MTS Minibionix 858) according to ASTM standard D1708 [34]. The specimen thickness ranged between 0.05 and 0.2 mm. Four replicates of each type of electrospun scaffold were obtained. The tests were

performed at a strain rate of 10 mm/min. The AN specimens were cut such that the applied load was parallel to the longitudinal axis of the aligned nanofibres. The load and displacement values during the tests were measured by a load cell (110 N) and a linear variable differential transformer (LVDT) (±50 mm), respectively; all data were registered by a virtual instrument programmed in LabVIEW [35].

Characterisation

The purpose of the characterisation was to correlate the structure of the nanofibres and scaffolds with the mechanical properties of the materials to support the elastic models.

External morphology of the electrospun nanofibres

A set of SEM micrographs of the PLA electrospun scaffolds is shown in Fig. 2. The degree of orientation of the ANs was analysed at two take-up collection velocities: 1100 m/min ($AN_{1100\ m/min}$) and 1217 m/min ($AN_{1217\ m/min}$). Figure 2a, b show that almost all the nanofibres are aligned along the tangential direction of the cylindrical rotating collector. Both the diameter and degree of alignment of the nanofibres were measured using ImageJ software. The average deviation of alignment was approximately ±3°. Therefore, it could be assumed that the nanofibres were uniaxially oriented. The average diameter of the $AN_{1100\ m/min}$ nanofibres was 643.8 ± 50 nm, with a high degree of nanofibre orientation (Fig. 2a) and smooth and homogeneous surfaces (Fig. 2b). The RONs scaffolds had a greater average diameter: 992 ± 257 nm (Fig. 2c), and the nanofibres showed a rough surface with considerable variation in diameter along the longitudinal axis (Fig. 2d). It can be concluded that the quality of the AN scaffolds is better than that of the RON scaffolds. The rotational collector not only orients the nanofibres but also stretches them to a regular diameter and surface.

The influence of the take-up velocity and annealing on the diameter of the nanofibres is depicted in Fig. 2e. The RONs (zero take-up velocity) presented the highest diameters and standard deviations. The $AN_{1100\ m/min}$ and $AN_{1217\ m/min}$ nanofibres without thermal treatment had diameters of 643 ± 50 and 747 ± 117 nm, respectively. These results were compared with those obtained by Inai et al. [20], who reported ANs of PLA collected at 6 and 630 m/min with average diameters of 890 ± 190 and 610 ± 50 nm, respectively. It is worthwhile to note that Inai's experimental electrospinning parameters were different from ours; however, despite the combination of different parameters, such as polymer concentration, feed rate, solution electroconductivity, take-up velocity and type of collectors used, the AN diameters in both studies are similar at velocities above 630 m/min. According to our results, take-up velocities above 1100 m/min did not influence the diameter of the nanofibres. In contrast to Inai et al. [20], we show that from 6 to 630 m/min (100-fold change in the velocity), there is a significant reduction in the diameter of the nanofibres.

The A-ANs showed the lowest average diameter. The $A\text{-}AN_{1100\ m/min}$ nanofibres showed an average diameter of 562.8 ± 210 nm, while the $A\text{-}AN_{1217\ m/min}$ nanofibres showed an average diameter of 525.8 ± 90.4 nm. By comparing the annealed and non-annealed nanofibres, a small decrease in the diameter was found, between 12 and 30 %, as shown in Fig. 2e. This behaviour is due to the self-assembly of the chain molecules in the nanofibre as a result of annealing. This effect was not observed in the RONs.

Figure 3a shows a phase AFM image of ANs prepared without annealing at a take-up velocity of 1217 m/min. Two well-defined alternating (periodic) dark and bright regions are easily observed on the electrospun nanofibre surface. The dark and bright regions correspond to lamellar and amorphous phases, respectively. These different phases were clearly identified by the phase AFM image, captured in tapping mode. This could be due to the difference in the sample hardness, density or the fibre orientation. Different regions of the sample were analysed by AFM with highly reproducible results. In the annealed samples, these observed features disappeared.

In general, the observed structure agrees with the previous model of Ciceron et al. [22], developed for the morphology of PLA microfibres produced by a melt spinning process. These results indicate that models for microfibrillar morphology could also be used for nanofibres.

The obtained AFM images may also provide a quantitative evaluation. The lamellar fraction (V_2) was identified and measured by Nanoscope v. 5.30 software, Veeco, USA. The evaluation was repeated ten times in different sample regions. The results indicate that the average lamellar volume fraction (V_2) occupies approximately 35.7 % of the $AN_{1217\ m/min}$ nanofibres.

The HRTEM image of an AN cross-section, prepared at a take-up velocity of 1217 m/min, is displayed in Fig. 3b, where amorphous core (bright region) and supramolecular shell (dark region) phases are clearly distinguished. This confirms the assumption of Arinstein et al. [21] regarding the formation of oriented polymeric chains (supramolecular structure) in the shell due to the electrospinning process. As discussed later, the consideration of this core–shell morphology is important for the prediction of the elastic properties of the nanofibres. The elastic properties of the core (amorphous) are assumed to be constant in contrast to

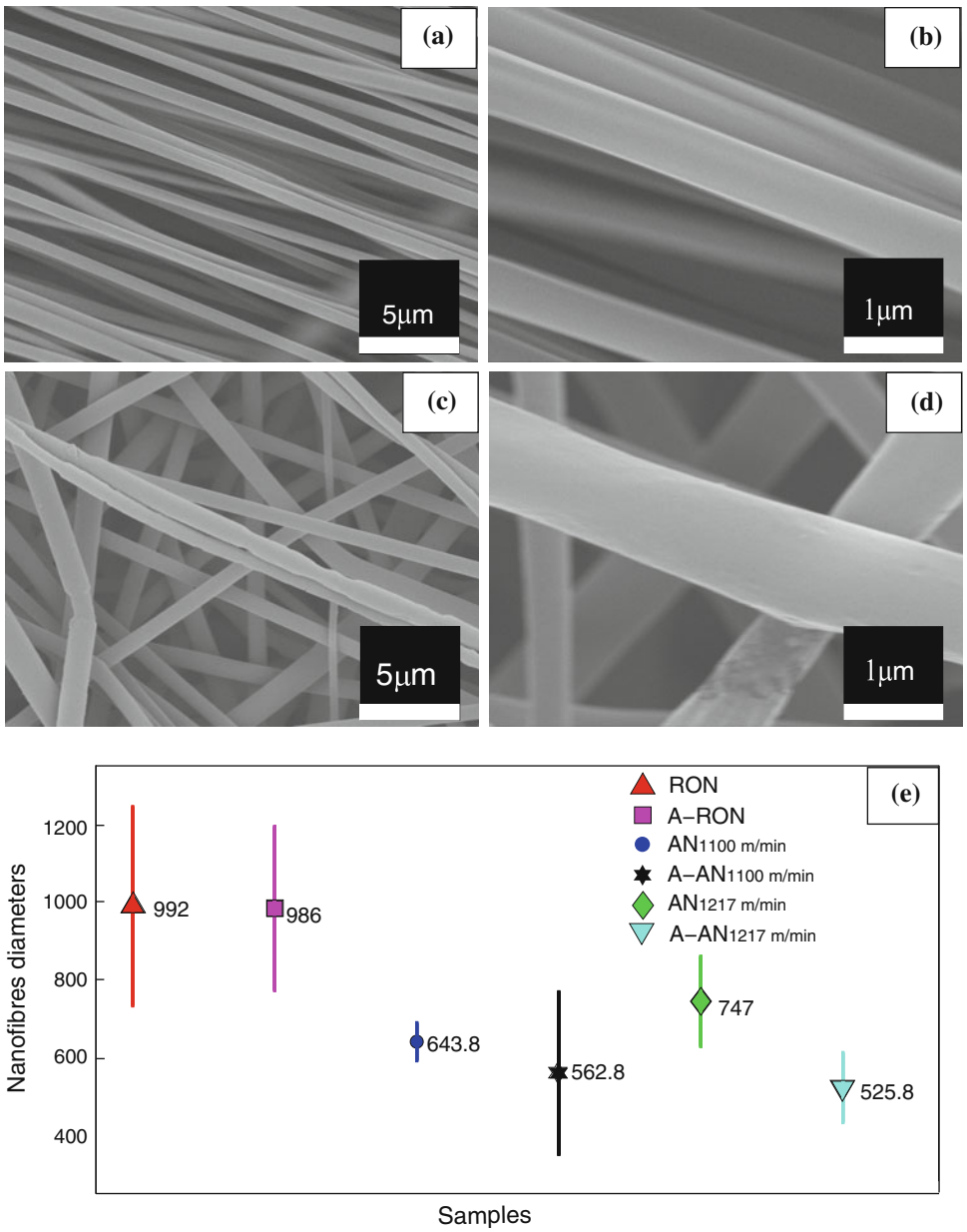

Fig. 2 SEM images of the electrospun PLA nanofibres. **a** Aligned nanofibres collected at 1100 m/min. **b** The same image as in **a** at higher magnification showing a smooth surface without pores or defects. **c** Random oriented nanofibres collected in a static square plate. **d** The same image as in **c** at higher magnification showing pores and defects on the surface. **e** The diameters of the different types of PLA nanofibres [randomly oriented nanofibre (RON), annealed randomly oriented nanofibre (A-RON), (AN) aligned nanofibre, and annealed aligned nanofibre (A-AN)] showing that the size was influenced by the alignment and heat treatment

the shell. As shown in Fig. 3a, the shell is composed of a supramolecular lamellar phase; therefore, the elastic properties may vary across it.

Crystallographic analysis

The XRD plots (Fig. 4) suggest that the level of atomic organisation of PLA is strongly dependent on the processing conditions. Bulk PLA, used as a reference, has a semicrystalline structure (purple plot line in Fig. 4a) with two characteristic peaks at 16.8° and 19.2° (Bragg angles). These results suggest a crystalline orthorhombic structure (according to PDF-2-2006 card number 00-054-1917, Diffract Plus 2005), with the following lattice parameters: $a = 10.61$ Å, $b = 6.05$ Å and $c = 28.8$ Å. The RONs have a typical amorphous structure (green plot line in Fig. 4a). The rapid solidification of the fibres during the electrospinning process precluded slow three-dimensional

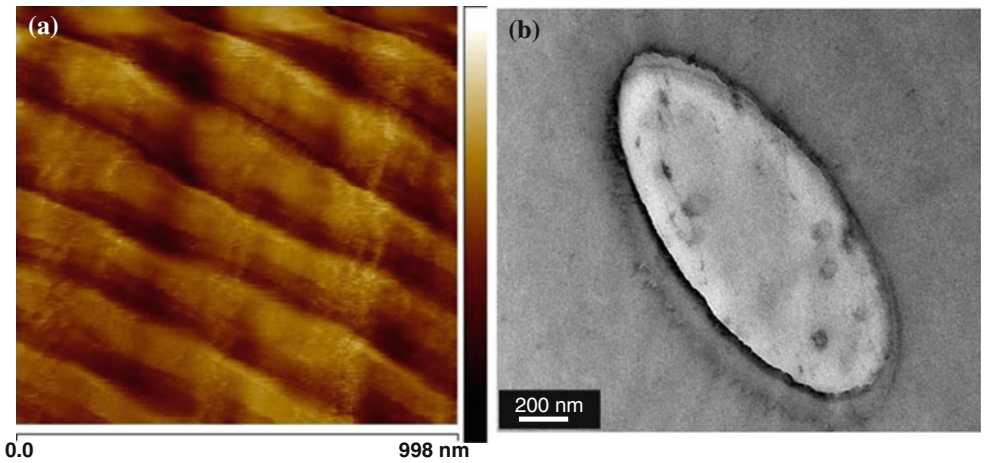

Fig. 3 Structure of an aligned PLA electrospun nanofibre. **a** Phase AFM image of the nanofibre surface. **b** HRTEM micrograph of the cross-section of the nanofibre

ordering at the atomic level of the PLA; therefore, no evidence of extensive crystallisation is observed. However, after the fibres are annealed below the melting point (A-RONs), a peak at 16.8° appears (red plot line in Fig. 4a). This result is clear evidence of the self-assembly of the polymer chains at the atomic level.

Figure 4b shows the XRD results of the ANs. There is no evidence of crystallinity in the $AN_{1100\ m/min}$ and $AN_{1217\ m/min}$ nanofibres, as depicted by the blue and black plot lines. However, as could be expected, annealing promotes extensive crystallisation of the polymer chains, as shown by the red and green plot lines; in both plots, the peak is observed at 16.8°. It is most likely that during the electrospinning, the AN polymer chains are oriented along the main axis of the nanofibres due to both the electrical field and winding at high speeds. However, the rapid solidification rate tends to inhibit the crystallisation of the polymer. Annealing promotes chain self-assembly, and as expected, the ANs develop a higher crystallinity than the RONs.

Thermal transitions

The thermal transitions of the electrospun nanofibres were studied by DSC to elucidate any trends in the crystallisation. The thermal transitions of the electrospun nanofibres are shown in Fig. 4c, d. The glass transition (T_g) and melting (T_m) temperatures were approximately equal in all cases: ($T_g = 60$ °C and $T_m = 147$ °C). Because the working temperature of the PLA scaffolds in the human body will be 23 °C, below its T_g (60 °C), structural modification of the nanofibres will not occur. Therefore, the PLA scaffolds can be safely used in tissue engineering. The PLA nanofibres also showed a crystallisation temperature (T_c) at 106–108 °C, which was affected by the take-up velocity.

Figure 4c shows the thermal transitions of the bulk PLA, RON and A-RON samples. The RON and A-RON samples showed an enthalpic relaxation due to the rapid solidification rate during electrospinning. This enthalpic relaxation temperature occurred at approximately 65 °C (endothermic peak). As expected, the degree of molecular disorder of the chains was higher in the RONs than in the A-RONs, as shown by the enthalpy values of 6.3 and 5.8 J/g, respectively.

As shown in Fig. 4c, the RONs and A-RONs exhibited exothermic peaks between 106 and 108 °C. These peaks, with enthalpy values of 19.4 and 23.1 J/g, respectively, correspond to the crystallisation of the polymer. The energy released during crystallisation was higher in the A-RONs because of the effect of annealing at 80 °C. Melting was observed at approximately 147 °C. Again, the melting peak of the A-RONs was more intense than that of the RONs, with enthalpies of 25.67 and 21.20 J/g, respectively, indicating a greater crystalline fraction in the A-RONs. The dual melting point in the RONs may be due to the coexistence of two phases in the nanofibres because the stretching during the fast electrospinning process may transform some α crystals into the β form, possibly disrupting the lamellar packing [36].

The thermograms of the ANs and A-ANs also show enthalpic relaxation peaks at approximately 65 °C, with enthalpy values of 5.8 J/g for both the $AN_{1100\ m/min}$ and $AN_{1217\ m/min}$ nanofibres. This value was similar to that observed in the RONs. After annealing, the relaxation enthalpies were smaller than in the A-RONs as follows: 5.8 J/g for the A-RONs, 4.5 J/g for the $A\text{-}AN_{1100\ m/min}$ nanofibres and 3.6 J/g for the $A\text{-}AN_{1217\ m/min}$ nanofibres. This tendency was also a confirmation that the combination of take-up velocity and annealing parameters improved the internal organisation of the polymer nanofibres.

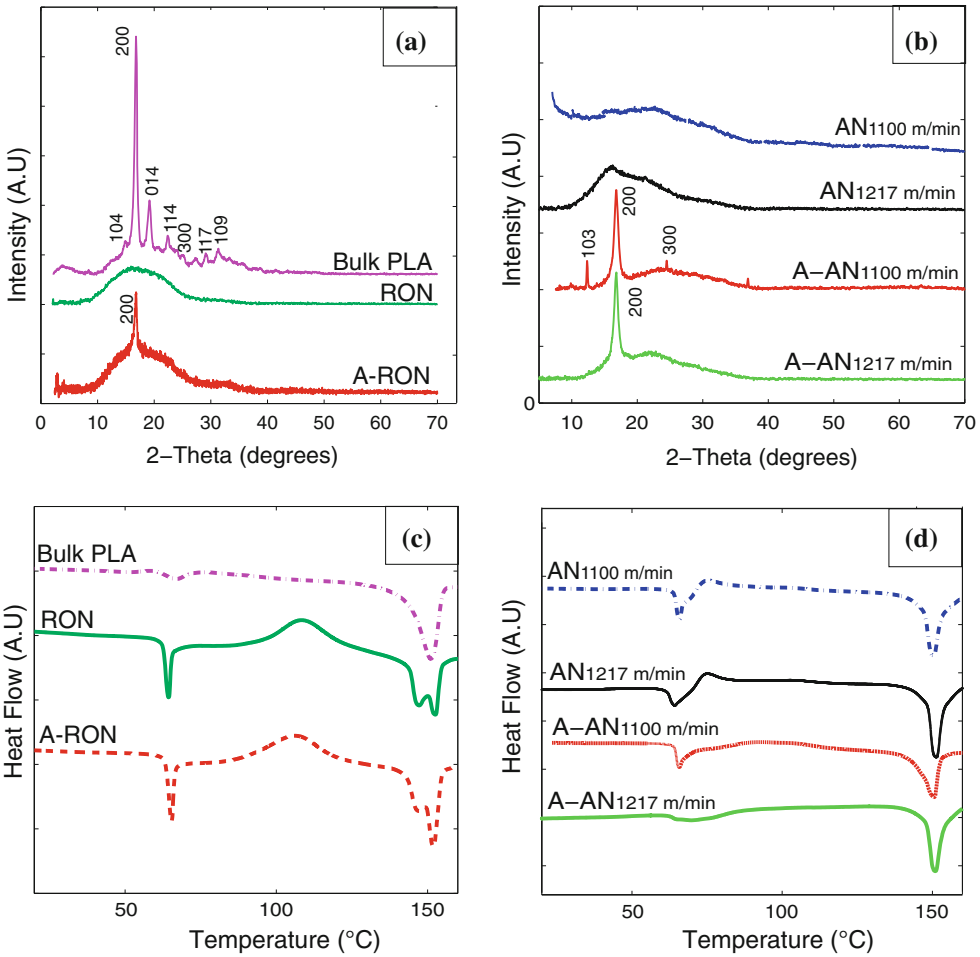

Fig. 4 XRD and DSC plots of PLA nanofibres. **a** Diffractograms of bulk PLA, RON and A-RON. **b** Diffractograms of AN and A-AN. **c** DSC of bulk PLA, RON and A-RON. **d** DSC of AN and A-AN

The ANs also showed crystallisation; in the case of the $AN_{1100\ m/min}$ nanofibres, the crystallisation peak was found at 75.3 °C with an enthalpy of 3.9 J/g, while in the $AN_{1217\ m/min}$ nanofibres, it was at 74.8 °C with an enthalpy of 4.6 J/g. The orientation of the nanofibres by the rotational collector induced a significant change in the crystallisation compared to the RONs; a reduction of approximately 30 °C in the crystallisation temperature (T_c) and smaller crystallisation enthalpies was observed, implying that the ANs required less energy to reach the crystalline state.

The $A\text{-}AN_{1100\ m/min}$ nanofibres showed a T_c of 92.6 °C with an enthalpy of 1.5 J/g, and the $A\text{-}AN_{1217\ m/min}$ nanofibres did not show a crystallisation peak. This result means that the A-ANs reached the maximum value of crystallinity after annealing. The obtained data indicate that annealing has a strong effect on both the crystallisation temperature and the crystalline structure of PLA nanofibres.

The melting temperatures of the ANs and the A-ANs were 146 and 148 °C, respectively. The enthalpy values of the $AN_{1100\ m/min}$ (28.63 J/g) and $AN_{1217\ m/min}$ (31.93 J/g) nanofibres are greater than those observed in the A-RONs (25.67 J/g) and RONs (21.20 J/g), indicating that the ANs and A-ANs possess a higher crystallinity due to the orientation of the polymer chains along the nanofibres.

In the case of the A-ANs, the melting enthalpy was greater for the fibres collected at 1217 m/min than those collected at 1100 m/min. The enthalpies of the $A\text{-}AN_{1100\ m/min}$ and $A\text{-}AN_{1217\ m/min}$ nanofibres were 18.47 and 29.84 J/g, respectively. These values indicate that a higher take-up velocity improved crystal formation. Our results showed a crystallisation peak, and the XRD analysis confirmed the amorphous-crystalline structure in the samples, as observed in Fig. 4. The electrospinning, nanofibre orientation, take-up velocity and annealing all promote self-assembly of the polymer chains.

According to the XRD evidence (Fig. 4a, b), the ANs were not crystalline before annealing. However, DSC revealed a crystallisation peak in the same type of samples. The XRD technique is not the most effective at detecting the small polymer crystalline structures in the nanofibres, compared to DSC. In addition, DSC is a very sensitive technique for detecting enthalpy changes, including those due to crystallisation. During the DSC experiments, the heating process induced the oriented polymer chain structures to form bigger crystals before melting.

Mechanical characterisation

The main objective of the mechanical characterisation is to study and model the elastic properties of the electrospun nanofibre scaffolds under uniaxial tension. The experimental data will be compared in the following section with the results obtained using theoretical models. Other important properties such as the yield strength σ_{ys} and the ultimate strength σ_{us} were also measured. The results are summarised in Table 2. The elastic modulus and the yield stress of the electrospun AN scaffolds were 7–9 and 10–13 times higher than the RON scaffolds, respectively. These differences in the elastic properties are explained in terms of the nanofibre and molecular orientation. In contrast to the RON scaffolds, the nanofibres in the AN scaffolds were oriented parallel to the load direction. Therefore, almost all the nanofibres supported and distributed the load simultaneously during the uniaxial tensile test.

As explained above, the polymer chain orientation was higher in the ANs than in the RONs due to the drawing of the nanofibres during the electrospinning of the ANs. The XRD and DSC studies also suggest that there is better molecular orientation in the ANs. As the polymer chains were oriented along the main axis of the nanofibres, the elastic modulus increased in the direction of the nanofibre because the covalent bonds among the carbon atoms in the polymer chain were stronger than the intermolecular bonds between polymer chains (Van der Waals, hydrogen bonding and others). In addition, the elastic modulus of the ANs drawn at 1217 m/min was higher than that of the ANs drawn at 1100 m/min.

Annealing at 80 °C had a small effect on the elastic properties of the ANs, as observed in Table 2. This result suggests that the change in the crystallisation was small and, therefore, did not affect the elastic properties.

During the course of the tensile tests, the nanofibres in the RON scaffolds were oriented along the applied load direction. During this process, some nanofibres failed, while others were aligned and supported the applied load until failure occurred. As a result, the RON scaffolds presented the smallest yield stress σ_{ys} and ultimate strength σ_{us} in comparison with the AN scaffolds. The nanofibres in the AN scaffolds possessed better morphology than the RON scaffolds, as shown in Fig. 2b, and thus had fewer defects and improved mechanical properties.

Mathematical models

The nano- and microstructures inferred above are used as a reference in the mathematical modelling. Various microstructural aspects of the nanofibres have been identified in the characterisation section using AFM, HRTEM, XRD, DSC and SEM techniques. To predict the mechanical effective properties of electrospun nanofibres of PLA across and along the length of a nanofibre, a composite made of two constituents and a simple geometrical arrangement is assumed. One is referred to as a Laminate Bimaterial Periodic Structure (LBPS), and the other as a Hierarchical Bimaterial Cylindrical Structure (HBCS). In both cases, two phases of PLA are present: amorphous and lamellar. These structures are modelled by the analytical models shown below, which adequately describe the morphology and the elastic behaviour of PLA nanofibres. These are the simplest models that comply with the structural and geometric characteristics of PLA nanofibres.

Laminated bimaterial periodic structure (LBPS)

The AFM image shown in Fig. 3a suggests a bimaterial repetitive cell that repeats widely over the length. The geometry in the mathematical model used is displayed in Fig. 5a. In the LBPS model, the elastic properties are assumed to be constant. The formulas given below are applicable [37, 38]. The elastic properties of the material correspond to an isotropic medium specified with only two constants, namely, Young's modulus E and Poisson's ratio v. Let V_1 and V_2 be the width of each material, so that $V_1 + V_2 = 1$, where subindices 1 and 2 are associated with the amorphous and lamellar phases, respectively. These moduli have a non-constant variation as shown in Fig. 5b. Note that V_1 can also be thought of as the volumetric fraction per unit area of the amorphous phase. The homogenised composite, on the other hand, is transversely isotropic and characterised by five independent parameters. Recently, Ramirez et al. [37] developed explicit

Table 2 Mechanical properties of the PLA scaffolds

Scaffolds type	Young's modulus E (MPa)	Yield stress σ_{ys} (MPa)	Yield strain max %	Ultimate stress σ_{us} (MPa)	Ultimate strain max %
RON	96.8 ± 32.5	1.7 ± 0.2	4.2 ± 2.4	2.8 ± 0.6	129.6 ± 32.5
$AN_{1100\ m/min}$	683.6 ± 33.2	18.4 ± 0.6	3.4 ± 0.3	24.0 ± 0.7	86.4 ± 15.2
A-$AN_{1100\ m/min}$	620.8 ± 74.2	13.8 ± 4.8	3.6 ± 0.4	20.3 ± 8.8	95.5 ± 10.0
$AN_{1217\ m/min}$	881.3 ± 100.2	25.0 ± 2.2	3.7 ± 0.4	32.2 ± 2.9	75.0 ± 7
A-$AN_{1217\ m/min}$	854.2 ± 60.7	19.4 ± 1.1	3.5 ± 0.7	31.0 ± 3.0	93.0 ± 4.9

formulas for this type of laminate structure, two of which are reproduced here as follows:

$$E_{\text{in}} = E_1V_1 + E_2V_2 + \left[\frac{V_2E_1E_2V_1\,(v_1 - v_2)^2}{\left(1 - v_1^2\right)\left(1 - v_2^2\right)}\right] \Big/ \left(\frac{E_1V_1}{\left(1 - v_1^2\right)} + \frac{E_2V_2}{\left(1 - v_2^2\right)}\right), \quad (1)$$

$$\frac{1}{E_{\text{out}}} = \frac{V_1}{E_1} + \frac{V_2}{E_2} - 2\left[\frac{V_2E_1E_2V_1}{(1 - v_1)(1 - v_2)}\left(\frac{v_1}{E_1} - \frac{v_2}{E_2}\right)^2\right] \Big/ \left(\frac{E_1V_1}{(1 - v_1)} + \frac{E_2V_2}{(1 - v_2)}\right), \quad (2)$$

where E_{in} and E_{out} are the in-plane and out-of-plane Young's moduli, respectively. It must be said that (1) and (2) are exact simple closed-form formulas. These expressions depend only on the volume fractions and elastic properties of each material.

Formulas (1) and (2) are calculated as a function of the volumetric fraction V_2 and plotted in Fig. 5a using MATLAB 2010®, where $E_{\text{amorphous}} = E_1 = 350$ MPa, $E_{\text{lamellar}} = E_2 = 2800$ MPa, $v_{\text{amorphous}} = v_1 = 0.45$ and $v_{\text{lamellar}} = v_2 = 0.35$ (data taken from previous reports) [39–41]. The analytical model is calculated for all lamellar volume fractions; In particular, attention is given to the value of 35.7 % obtained by AFM, in which case E_{out} equals 667 MPa for PLA nanofibres.

Well-known rules of mixtures and simple E_{Voigt} and inverse E_{Reuss} [38] are also given below and plotted in Fig. 6a as a reference.

$$E_{\text{voigt}} = (E_1V_1) + (E_2V_2), \quad (3)$$

$$\frac{1}{E_{\text{Reuss}}} = (V_1/E_1) + (V_2/E_2) \quad (4)$$

The latter is a well-known lower boundary of E_{out}. Note that the left-hand side of (2) is greater than E_{Reuss}, and the left-hand side of (1) is also greater than E_{Voigt} due to the positivity of the second term of the equation.

Hierarchical bimaterial cylindrical structure (HBCS)

Studies by other authors suggested that the nanofibre structure could be hierarchical (Fig. 5c) [11, 18, 19, 21]. Our experimental studies (XRD, DSC, SEM and especially HRTEM) support this theory that the most likely internal nanofibre structure is hierarchical. The inset in Fig. 5c shows a small length nanofibre as a cylindrical structure composed essentially of two parts, an internal core and an external shell. The core is considered an amorphous phase, whereas the shell can be composed of parallel nanofibrils oriented along the axis of the cylinder. This shell is also reported as a supramolecular

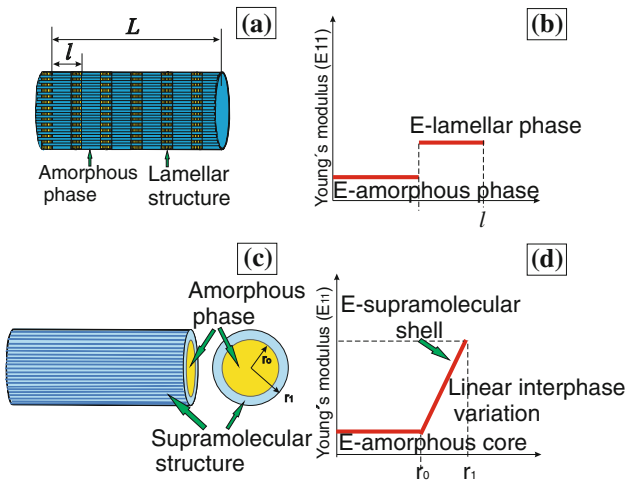

Fig. 5 Aligned nanofibre structure models and corresponding schemes of mechanical behaviour. **a** Composite nanofibre showing a laminate structure. **b** Young's modulus of an amorphous-lamellar cell in a laminated material. **c** Composite nanofibre with a core–shell hierarchical structure. **d** Young's modulus behaviour according to the hierarchical model with linear interphase variation of the shell between the core and surface

structure in nanofibres [18, 21]. Therefore, this core–shell structure will be modelled by the HBCS assumption.

The HBCS model considers two phases: amorphous (core) and supramolecular (shell). These two phases present functional interphase variations between them. The changes that occur between the amorphous and supramolecular surfaces in polymeric fibres could be gradual, due to stretching and bending instabilities that affect the orientation of the molecular chains on the surface; this effect decreases closer to the core [8, 17, 21]. The surface of the shell was observed by AFM (see Fig. 3a). In HBCS, the properties of the core are constant, but those of the shell vary linearly.

The DRM allows us to model interphases by considering the amorphous phase as an inclusion with an inhomogeneous interphase (the supramolecular one), as shown in Fig. 5d. Experimentally, it is difficult to characterise the interphase; we considered linear interphase variation because this variation is physically possible. The application of the DRM by Shen and Li [31, 32] uses the well-known Mori–Tanaka formulas at the outset to obtain effective first-order differential equations that are easily solved. Here, the starting set of formulas is the following longitudinal Young's modulus E_{11}, major Poisson's ratio v_{12} and plane bulk modulus K_{23}, given as follows:

$$E_{11} = V_1E_1 + (1 - V_1)E_s + \frac{4V_1(1 - V_1)(v_1 - v_s)^2\mu_s}{\left[\frac{(1-V_1)\mu_s}{(K_1 - \frac{\mu_1}{3})}\right]\left[\frac{V_1\mu_s}{(K_s - \frac{\mu_s}{3})}\right] + 1} \quad (5)$$

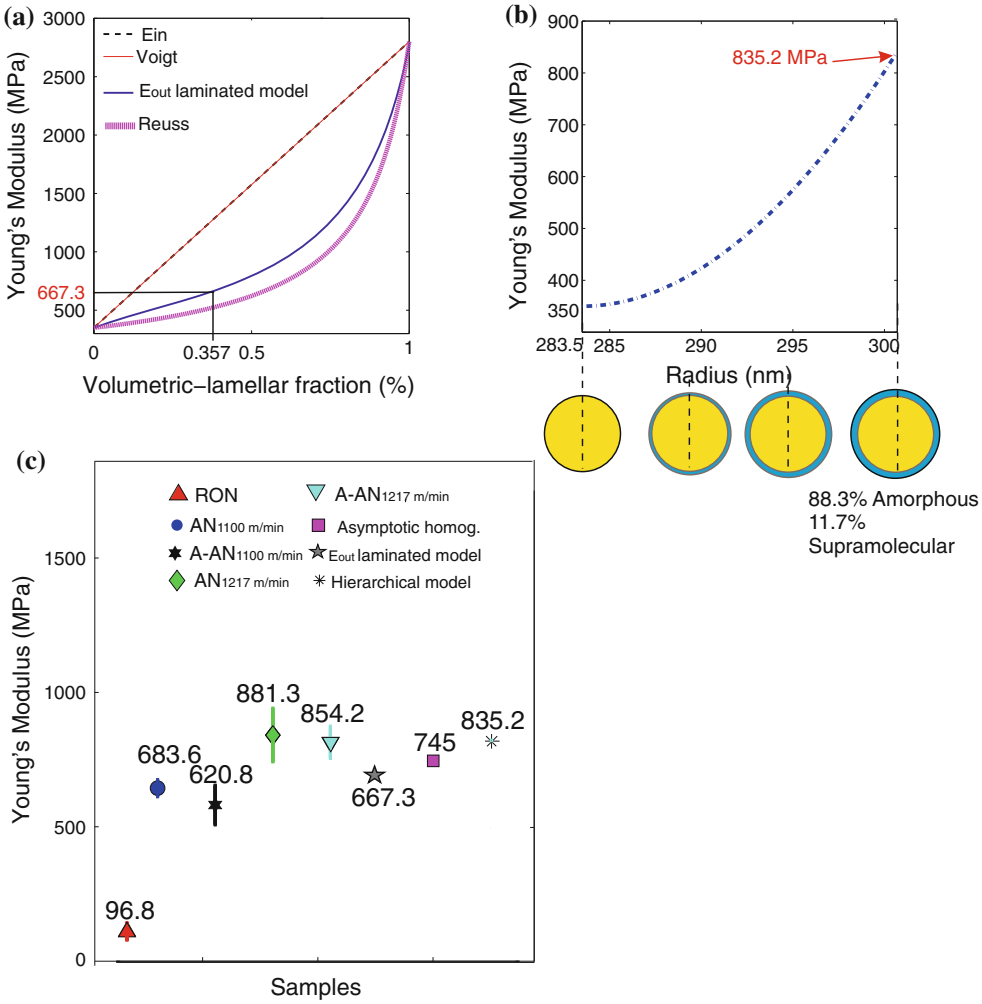

Fig. 6 Theoretical and experimental Young's moduli for PLA electrospun nanofibres. **a** Results of the LPBS model of nanofibre as a function of lamellar volume fraction compared with other approximations. **b** Results of the hierarchical model as a function of the radius of the interphase. **c** Comparison of the Young's modulus between the experimental results and model predictions for PLA nanofibres

$$v_{12} = (1 - V_1)v_s + V_1 v_1 + \frac{V_1(1 - V_1)(v_1 - v_s)\left[\left(\frac{\mu_s}{(K_s - \frac{\mu_s}{3})}\right) - \left(\frac{\mu_s}{(K_1 - \frac{\mu_1}{3})}\right)\right]}{\left(\frac{(1-V_1)\mu_s}{(K_1 - \frac{\mu_1}{3})}\right) + \left(\frac{V_1\mu_s}{(K_s - \frac{\mu_s}{3})}\right) + 1} \quad (6)$$

$$K_{23} = K_s + \frac{\mu_s}{3} + \frac{V_1}{\left(\frac{1}{K_1 + K_s + \frac{1}{3}(\mu_1 - \mu_s)} + \frac{1 - V_1}{K_s + \frac{4\mu_s}{3}}\right)} \quad (7)$$

where μ and K_{23} are the longitudinal shear modulus and bulk modulus, respectively, for each material. K_{23} for each phase is defined as $K_1 - \mu_1/3$ and $K_s - \mu_s/3$; here subindices 1 and s are associated with the core (amorphous, the same used in the laminar case) and shell (supramolecular) phases. Equations (5)–(7) were first obtained by Hashin–Rosen for a cylindrical assemblage and are taken from Christensen [42]. By following the homogenisation method of the DRM according to Shen and Li [31, 32], the following initial value problem of the coupled first-order differential equations system is obtained:

$$\frac{dK_{23}}{dr} = \frac{-2}{r}\left[\frac{3\left[K_{23} - K_i + \left(\frac{1}{3}\right)(\mu_{12} + \mu_i)\right]\left[K_{23} + \frac{1}{3}\mu_{12} - \mu_i\right]}{(3K_i + \mu_i)}\right], \quad K_{23}(r_0) = K_{23\_1}, \quad (8)$$

where $K_{23\_s} = K_s - \frac{\mu_s}{3}$,

$$\frac{dv_{12}}{dr} = \frac{-2}{r}\left[(v_{12} - v_i) - \frac{(v_{12} - v_i)3\mu_i(3K_{23} + \mu_{12} - 3K_i - \mu_i)}{(4\mu_i + 3K_i)(3K_{23} + \mu_{12})}\right], \quad v_{12}(r_0) = v_1 \quad (9)$$

$$\frac{dE_{11}}{dr} = \frac{-2}{r}\left[(E_{11} - E_i) - \frac{\left(12K_i\mu_i + 4\mu_i^2\right)(v_{12} - v_i)^2}{(4\mu_i + 3K_i)}\right], \quad E_{11}(r_0) = E_1 \quad (10)$$

where r_0 and r_1 are the radius of the core and nanofibre, and the constant isotropic properties are E_{11}, v_{12}, μ_{12}, and

K_{23} (note that only two of them are necessary to characterise the rest). In these expressions, E_{11} is Young's modulus along the longitudinal direction, v_{12} is the major Poisson's ratio, μ_{12} is the longitudinal shear modulus and K_{23} is the plane bulk modulus, using as a reference a transversely isotropic notation even though the medium is isotropic. The subindex i refers to the elastic properties, again using a transversely isotropic notation, of the interphase, or the supramolecular phase, which has a radial dependence, i.e. K_i,

v_i, μ_i, E_i of width $h_f = r_1 - r_0$. Here, a linear interphase variation is assumed for each (see Fig. 5d). Other radial dependences could be modelled as well; here the simplest variation is considered as follows:

$$E_i = (E_s - E_1)\left(\frac{r - r_0}{hf}\right) + E_1 \tag{11}$$

$$K_i = (K_{23\_s} - K_{23\_1})\left(\frac{r - r_0}{hf}\right) + K_{23\_1} \tag{12}$$

$$K_{23\_s} = K_s - \frac{\mu_s}{3}$$

$$\mu_i = (\mu_s - \mu_1)\left(\frac{r - r_0}{hf}\right) + \mu_1 \tag{13}$$

Replacing the terms E_i, K_i and μ_i in Eqs. (8)–(10) allows us to observe the interphase effect on the elastic behaviour. This system can be easily solved by integration as an initial value problem with the software Matlab2010@. The required inputs for these equations are as follows: Young's modulus of the amorphous core ($E_1 = 350$ MPa); $v_1 = 0.45$ and $v_s = 0.35$, which are Poisson's coefficients for each phase [40, 41]. v_I was considered to be 0.4 (the average between the amorphous and supramolecular phases).The data used for the Young's modulus of the supramolecular shell are taken from ref. 39, which based the estimates on molecular dynamics calculations ($E_S = 9000$ MPa). These data are consistent with the experimental evidence that indicates the improvement of the Young's modulus due to the orientation of the polymer chains. This makes it plausible that the Young's modulus of these chains is greater than that for the bulk polymer.

Let us consider first the laminate model results. Fig. 6a displays a plot of the longitudinal Young's modulus E_{11} against the lamellar volume fraction V_2. It shows the results using the laminate model formula (1) and (2) and mixture rules (3) and (4). The variation in the Young's modulus is displayed as a function of the lamellar volume fraction in Fig. 6a. The general behaviour of E_{11} is that it increases monotonically. It can be observed that there is no difference between E_{in} and E_{Voigt}. E_{Reuss} is well-known to be a lower boundary for any composite biomaterial, independent of the geometry.

Considering a 35.7 % lamellar volumetric fraction for PLA nanofibre, the effective Young's modulus obtained with the laminated model is $E_{out} = 667$ MPa (see Fig. 6a). Comparing the theoretical and experimental results—polymer networks of $AN_{1100\ m/min}$ (683 MPa) and $AN_{1217\ m/min}$ (881.3 MPa)—it appears that E_{out} provides a better approximation for the first experimental value than the others: 505 and 1235 MPa for the Reuss and Voigt approximations, respectively.

Fig. 6b shows the Young's modulus as a function of the supramolecular phase radius r; the amorphous core radius is $r_0 = 283.5$ nm, and the shell thickness is $h_f = 17.1$ nm. The analysis shows the Young's modulus monotonically increasing due to the addition of supramolecular layers around the amorphous core of the PLA electrospun nanofibres. Therefore, as the supramolecular phase thickness increases, the percentage of amorphous phase decreases. This fact is shown in Fig. 6b schematically at the bottom of the figure, but it is not displayed to scale.

The effective Young's modulus obtained with DRM is 835.2 MPa. This value was nearer to the experimental value of 881.3 MPa. Consequently, this model is considered to be an excellent approximation.

Fig. 6c summarises the Young's modulus obtained for each theoretical value and also the experimental results. RON presented the lowest Young's modulus, as mentioned previously. $AN_{1100\ m/min}$ and $AN_{1217\ m/min}$ without thermal treatment showed better results than A-AN. The two theoretical models presented, E_{out} and the hierarchical model, show excellent predictive power, as they lie in the range of experimental values between 683.6 and 881.3 MPa for AN. E_{out} is statistically the same as $AN_{1100\ m/min}$: 667.3 and 683.5 MPa, respectively. Similarly, the hierarchical model is statistically equal to $AN_{1217\ m/min}$: 835.2 and 881.3 MPa, respectively. Although E_{out} is an approximation based on a one-dimensional composite such as laminate, its predictive power is rather good. The hierarchical model also showed excellent predictive power.

These results were compared with those obtained by Inai et al. (2005) [20] for AN of PLA collected at 6 and 630 m/min; these had an average Young's modulus between 1 and 2.9 GPa, respectively. Inai's experimental parameters were different, but the value of 1 GPa was very close to our results (881 MPa). Moreover, our theoretical and experimental results coincide with those of Inai et al. in that the increase of the take-up velocity in the collection (1100–1217 m/min) increases the Young's modulus, as observed in Fig. 6c.

Conclusions

The morphology and elastic properties of scaffolds of electrospun PLA nanofibres depend strongly on the take-up velocity and annealing conditions; winding the electrospun nanofibres in the rotational collector produced highly ANs. The morphology of the ANs was without defects and more

homogeneous in diameter than the RON scaffolds because of nanofibre stretching. This fibre stretching produced a high degree of self-assembly and an increase in the elastic properties.

The molecular orientation also increases with the take-up velocity; however, the rapid solidification that occurred during electrospinning limited the size of the crystalline structures. Annealing promoted better molecular self-assembly in the nanofibres, increasing the size of the crystals and the degree of crystallisation. The AN scaffolds have a hierarchical core–shell structure, where the core is amorphous and the shell has a supramolecular morphology, as observed by HRTEM. The surface of the nanofibres contains two periodic phases: the lamellar and amorphous, as observed by AFM.

By considering the morphology of the oriented nanofibres, both the Laminated Biomaterial Periodic Structure and the Hierarchical Biomaterial Structure models sufficiently predict the Young's modulus of the electrospun PLA nanofibres. The LBPS model (667 MPa) is better than the models based on the rule of mixtures: Reuss and Voigt predicted values of 505 and 1232 MPa, respectively. The Young's modulus value yielded by the model supported by HBCS and DRM (835 MPa) is in close agreement with that measured in the aligned nanofibre scaffolds (685–880 MPa).

Acknowledgements The authors thank Omar Novelo Peralta for SEM analysis, Patricia Castillo Ocampo for TEM analysis, Adriana Tejeda Cruz for XRD analysis, Damaris Cabrero Palomino for DSC analysis and Ana Pérez Arteaga and Ramiro Chávez for computational support. This project has been supported by ICyTDF (Grant 180/2009), DGAPA-UNAM (Grants IN116809 and IN108913), CONACYT (Grant 129658 and a scholarship), and PCeIM-UNAM.

References

1. Barnes CP, Sell SA, Boland ED, Simpson DG, Bowlin GL (2007) Adv Drug Deliv Rev 59:1413
2. Jayaraman K, Kotaki M, Zhang Y, Mo X, Ramakrishna S (2004) J Nanosci Nanotechnol 4:52
3. Agarwal S, Wendorff JH, Greiner A (2008) Polymer 49:5603
4. Yi-Fan G, Imran S, Rafaqat H (2013) J Mater Sci 48:3027. doi:10.1007/s10853-013-7145-8
5. Lannutti J, Reneker D, Ma T, Tomasko D, Farson D (2007) Mater Sci Eng, C 27:504
6. Liao S, Murugan R, Chan CK, Ramakrishna S (2008) J Mech Behav Biomed Mater 1:252
7. Persson M, Cho S-W, Skrifvars M (2013) J Mater Sci 48:3055. doi:10.1007/s10853-012-7022-x
8. Reneker DH, Yarin AL (2008) Polymer 49:2387
9. McClure M, Simpson DG, Bowlin GL (2012) J Mech Behav Biomed Mater 10:48
10. Hong Z, Qiu X, Sun J, Deng M, Chen X, Jing X (2004) Polymer 45:6699
11. Vera-Graziano R, Maciel-Cerda A, Moreno-Rondon EV, Ospina A, Gomez-Pachon EY (2012) Mater Res Soc Symp Proc 1376:1
12. Liao C-C, Wang C-C, Chen C-Y (2011) Polymer 52:4303
13. Tan EPS, Lim CT (2004) App Phys Lett 84:1603
14. Lim CT, Tan EPS, Ng SY (2008) App Phys Lett 92:3
15. Tan EPS, Lim CT (2006) Nanotechnology 17:2649
16. Wong S-C, Baji A, Leng S (2008) Polymer 21:4713
17. Naraghi M, Arshad SN, Chasiotis I (2011) Polymer 52:1612
18. Baji A, Mai Y, Wong S, Abtahi M, Chen P (2010) Compos Sci Technol 70:703
19. Yoshioka T, Dersch R, Tsuji M, Schaper AK (2010) Polymer 51:2383
20. Inai R, Kotaki M, Ramakrishna S (2005) Nanotechnol 16:208
21. Arinstein A, Burman M, Gendelman O, Zussman E (2007) Nat Nanotechnol 2:59
22. Cicero JA, Dorgan JR (2002) J Polym Environ 9:1
23. Stylianopoulos T, Barocas VH (2007) Comp Meth Appl Mech Eng 196:2981
24. Stylianopoulos T, Bashur CA, Goldstein AS, Guelcher SA, Barocas VH (2008) J Mech Behav Biomed Mater 1(4):326
25. Sun L, Han RPS, Wang J, Lim CT (2008) Nanotechnology 19:455706
26. Hori M, Nemat-Nasser S (1999) Mech Mater 31:667
27. Hill R (1964) J Mech Phys Solids 12:199
28. Hashin Z, Rosen BW (1964) J Appl Mech 31:223
29. Qiu YP, Weng GJ (1991) ASME J Appl Mech 58:388
30. Jasiuk I, Kouider MW (1993) Mech Mater 15:53
31. Shen L, Li J (2003) Int J Solids Struct 40:1393
32. Shen L, Li J (2005) Proc R Soc Lond A 461:1475
33. Sevostianov I, Kachanov M (2007) Int J Solids Struct 44:1304
34. ASTM D1708.10 (2010) Standard test method for tensile properties of plastics by use of microtensile specimens. doi:10.1520/D1708-10
35. Sánchez-Arévalo FM, Pulos G (2008) Mater Charact 59:1572
36. Montes De Oca H, Ward IM (2007) J Polym Sci Part B 45:892
37. Ramírez M, Nava-Gómez GG, Sabina FJ, Camacho-Montes H, Guinovart-Díaz R, Rodríguez-Ramos R, Bravo-Castillero J (2012) Int J Eng Sci 58:95
38. Milton GW (2002) The Mathematical Theory of Composites. Cambridge University Press, Cambridge
39. Garlotta D (2001) J Polym Environ 9:63
40. Gunatillake PA, Adhikari R (2003) Eur Cell Mater 5:1
41. Madhavan K, Nair NR, John RP (2010) Bioresour Technol 101:8493
42. Christensen RM (1991) Mechanics of composite materials edit. Krieger, Malabar